

Supplementary Information

Solvent-dependent structure of molecular iodine probed by picosecond X-ray solution scattering

Kyung Hwan Kim, Hosung Ki, Jae Hyuk Lee, Sungjun Park, Qingyu Kong, Jeongho Kim, Joonghan Kim, Michael Wulff, and Hyotcherl Ihee

1. TRXL Data collection

The principle of time-resolved X-ray liquidography experiment is shown schematically in Fig. 1 in the main text. The TRXL measurement was performed by using the laser pump–X-ray probe scheme at the beamline ID09B at ESRF. Laser pulses with the center wavelengths of 400 nm and 520 nm were generated by second harmonic generation and optical parametric amplification, respectively, of the output pulses from an amplified Ti:Sapphire laser system of 1 kHz repetition rate. The laser pulses were stretched to ~2 ps by passing through fused silica rods to avoid multiphoton excitation of the sample. The laser beam was focused by a lens to a circular spot of 120 μm diameter, where the laser beam overlaps with the X-ray beam at the crossing angle of 10° . The time-delayed X-ray pulses with the center wavelength of 0.68 \AA and ~3 % energy bandwidth were used as a probe without monochromatization. The effect of polychromaticity on scattering patterns was properly corrected by the polychromatic correction procedure. Two-dimensional (2D) scattering patterns were collected with an area detector (MarCCD) with a sample-to-detector distance of 40 mm and an exposure time of 4 s. Subsequently, one-dimensional (1D) scattering curves were obtained by azimuthal averaging of the 2D scattering patterns. To explore the solvent dependence of the molecular structure of molecular iodine, we used solution samples in two different solvents (methanol and cyclohexane). The solution sample was prepared by dissolving I_2 (Aldrich, 99.8%) in methanol

or cyclohexane at 10 mM concentration and was circulated through a high-pressure slit nozzle (0.3 mm slit, Kyburz) to form a stable liquid jet. Scattering patterns of the I₂ solution measured before (that is, -5 ns time delay) and after laser excitation were subtracted from each other to remove the contributions from non-reacting molecules. The resultant difference scattering curves were measured at the following time delays: -5 ns, -100 ps, 100 ps, 300 ps, 700 ps, 1 ns, 3 ns, 7 ns, 10 ns, and 1 μs. To achieve high signal-to-noise ratio enough for accurate data analysis, more than 20 images were acquired and averaged at each time delay.

2. Data processing

As mentioned above, an one-dimensional (1D) scattering curve, $S(q,t)$, was obtained by azimuthal averaging of a 2D scattering pattern as a function of momentum transfer $q = (4\pi/\lambda)\sin(\theta)$, where λ is the wavelength of X-rays, 2θ is the scattering angle, and t is the time delay between the laser and X-ray pulses. Difference scattering curves were generated by subtracting the reference data measured at -5 ns from the data at various positive time delays.

To get a more intuitive picture of the structural change, the difference scattering curves, $q\Delta S(q,t)$, can be converted into difference radial distribution functions (RDFs), $r\Delta S(r,t)$, in r -space by sine-Fourier transformation using the following equation:

$$r\Delta S(r,t) = \frac{1}{2\pi^2} \int_0^\infty q\Delta S(q,t) \sin(qr) e^{-q^2\alpha} dq \quad (1)$$

where the constant α is a damping term that accounts for the finite q range in the experiment and we used the value of $\alpha = 0.03 \text{ \AA}^2$.

3. Molecular Dynamics simulation

All the MD simulations were performed by following the protocols described in our previous publications¹⁻² using the program MOLDY.³ The periodic boundary conditions were used with a cubic box of 32.6 Å size containing one solute molecule embedded in 512 methanol molecules. This condition satisfies the density of methanol at standard temperature and pressure. The molecules were kept rigid. For the description of methanol solvent, we used the H1 model.⁴ The charges on individual atoms were obtained by DFT calculation and were kept fixed during

the simulation. The radial distribution functions (RDFs) were calculated up to 20 Å with 0.02 Å steps and used for the calculation of the scattering intensity.

4. Theoretical X-ray scattering intensities

Theoretical X-ray scattering curves were calculated using standard diffuse X-ray scattering formulas. The theoretical difference X-ray scattering curves, $\Delta S(q,t)_{\text{theory}}$, of the solution sample are composed of three components: (i) solute-only term, (ii) solute–solvent cross term, and (iii) solvent-only term as in the following equation:

$$\begin{aligned} \Delta S(q,t)_{\text{theory}} &= \Delta S(q,t)_{\text{solute-only}} + \Delta S(q,t)_{\text{solute-solvent}} + \Delta S(q,t)_{\text{solvent-only}} \\ &= \left[\sum_k c_k(t) S_k - S_g(q) \sum_k c_k(0) \right] + (\partial S / \partial T)_\rho \Delta T(t) + (\partial S / \partial \rho)_T \Delta \rho(t) \end{aligned} \quad (2)$$

where k is the index of the solute species, $c_k(t)$ is the fractional concentration of each solute species as a function of time t . The solute-only term was calculated by using the following Debye equation:

$$S(q) = F_1^2(q) \frac{\sin qR_{\text{I-I}}}{qR_{\text{I-I}}} \quad (3)$$

where F_1 is the atomic form factor of an iodine atom and $R_{\text{I-I}}$ is the I–I distance. In the structural fitting analysis presented below, $R_{\text{I-I}}$ was used as a fitting parameter that is freely variable to determine the molecular structure of I_2 in solution accurately. The solute–solvent cross term was calculated by the Debye equation using the pair distribution functions obtained from MD simulation. The solvent-only term was obtained by a separate solvent heating experiment by following the protocols detailed in our previous publication.⁵ Briefly, the pure solvent was excited by near-IR laser pulse and the scattering signal arising from temperature jump and subsequent thermal expansion was measured and used for the analysis.

5. Fitting & error analysis

The experimental scattering curves were fitted by theoretical scattering curves using the maximum likelihood estimation (MLE) with chi-square (χ^2) estimator. For the fitting analysis,

we used four variable parameters: I–I distance, rate constant for nongeminate recombination, quantum yield, and scaling factor. The chi-square estimator is given by the following equation:

$$\chi^2(R_{I-I}, k_1, Q, A) = \frac{1}{N-p-1} \sum_i \frac{(\Delta S_{theory}(q_i) - \Delta S_{exp}(q_i))^2}{\sigma_i^2} \quad (4)$$

where N is the total number of q points (= 960 for our experimental data), p is the number of fitting parameters (= 4 without any constraint), and σ_i is the standard deviation at i^{th} q -point. The likelihood (L) is related to χ^2 by the following equation:

$$L(R_{I-I}, k_1, Q, A) \propto \exp(-\chi^2/2) \quad (5)$$

The errors of the multiple fitting parameters were determined from this relationship by calculating the boundary values at 68.3% of the likelihood distribution. The calculation was performed by MINUIT software package and the error values were provided by MINOS algorithm in MINUIT. More details of the error analysis can be found in our previous publication.⁶

6. Computational details of DFT calculations

All molecular structures were optimized using the density functional theory (DFT) method. Subsequently, harmonic vibrational frequency calculations were performed on the optimized molecular structures. We used long-range corrected DFT functional, ω B97XD,⁷ which also contains an empirical dispersion term. To treat the scalar relativistic effect of iodine atoms, we used the dhf-TZVPP,⁸ small-core relativistic effective core potential (RECP) with the triple- ζ basis set for the valence electrons. For other atoms (C, O, and H), 6-31+G(d) basis sets were used. For implicit treatment of the solvent environment, we used the integral-equation-formalism polarizable continuum model (IEFPCM) method.⁹ To treat solvent molecules explicitly, the molecular structure of I_2 was optimized with a total of 22 surrounding explicit methanol molecules in the first solvation shell around an I_2 molecule. To examine the potential energy curves of the I_2 while varying the I–I bond length, we performed the scan calculations for both isolated I_2 and I_2 inside a methanol cluster. In the latter case, the relaxed scan calculations was carried out for the I–I bond. We used the natural population analysis (NPA) for characterizing

the atomic charge of iodine atoms. All DFT calculations were performed using the Gaussian09 program.

7. Photodissociation kinetics of I₂ in methanol

Time-resolved difference scattering curves, $q\Delta S(q,t)$, measured for photodissociation of I₂ in methanol at time delays from 100 ps to 1 μ s are shown in Figure S2A. To have a more intuitive picture of structural changes in real space, the difference scattering curves in q -space, $q\Delta S(q,t)$ can be converted into difference radial distribution functions (RDFs) in real space, $r\Delta S(r,t)$, by sine-Fourier transformation. The difference RDFs shown in Figure S2B represent the change of interatomic distances (r) in the molecules participating in the reaction.

According to previous studies on photodissociation of I₂ in solution using time-resolved spectroscopy¹⁰⁻¹¹ and TRXL,^{2, 12} the photodissociated iodine atoms recombine either geminately (by relaxation through the A/A' state or vibrational cooling in the X state) or nongeminately (by slow diffusion). To elucidate the detailed reaction mechanism of photodissociation of I₂ in methanol, we analyzed our TRXL data by considering both geminate and nongeminate recombination processes as shown in Figure S4. Details of the fitting and error analysis are given in the previous sections.

The results of the fitting analysis are shown in Figures S2 and S3. Since the shape of the oscillatory features stays almost the same up to 10 ns and only the signal intensity decreases over time, we can infer that nongeminate recombination is dominant in the time range of our measurement while the contribution of geminate recombination is negligible. In fact, when we consider both geminate and nongeminate recombination in the TRXL fitting analysis, we found that the contribution of geminate recombination converge to zero within the error range. However, this result does not necessarily mean that geminate recombination by relaxation through the A/A' state or vibrational cooling in the X state does not occur. Considering the results of previous studies on I₂ in other solvents,^{2, 12} it is more likely that geminate recombination is much faster than 100 ps and cannot be observed in the time range of our measurement.

From the analysis of the time-resolved difference scattering data, we obtained time-dependent concentration changes of transient solute species (iodine radical and I₂ molecule) as shown in Figure S3A. We can see that 18 ± 2 % of photoexcited I₂ molecules dissociate into two iodine atoms in less than 100 ps after photoexcitation. Then, the parent I₂ molecule is regenerated by nongeminate recombination in ~ 10 ns. The non-reacting portion (82 ± 2 %) of the photoexcited I₂ molecules returns to the ground state within 100 ps by geminate recombination via the relaxation through the A/A' state or vibrational cooling of X state. The reaction mechanism of the photodissociation of I₂ and the time scales of individual reaction steps determined from our analysis are summarized in Figure S4. Besides the concentration dynamics, we also obtained the information on the temperature change and volume expansion of the solvent environment as shown in Figure S3B. The non-dissociating portion of the photoexcited I₂ molecules dissipate the heat to the solvent environment, leading to the temperature increase by 0.48 K in the excited volume at early time delays. Then, volume expansion of the excited volume occurs at late time delays after 10 ns, resulting in the decrease of the solvent density by 0.64 kg/m³.

8. Transient structure of solute/solvent cage and the changes in solvent density and temperature

Since X-rays scatter off every atom in a molecule, the TRXL measurement is sensitive to not only structural changes of solute molecules but also solute–solvent interaction (cage term) and solvent hydrodynamics. Therefore, the TRXL measurement can reveal the transient structure of the solute–solvent cage and the change in temperature and volume of the solvent in addition to the structural dynamics of solute molecules. To distinguish the components of different origins constituting the TRXL signal, the difference RDFs in real space, $r\Delta S(r,t)$, can be decomposed into three components: (a) the solute-only term, (b) the cage term, and (c) the solvent-only term. The decomposed difference RDFs for photodissociation of I₂ in methanol are shown in Figure S4. At the bottom of each plot, the distances of major atom-atom pairs are indicated as lines. The lines above the baseline correspond to the positive contributions reflecting the formation of reaction intermediates and products as well as the change in their associated solvent environment,

while the lines below the baseline correspond to the negative contributions reflecting the depletion of the reactant (I_2 molecule) and the change in its related solvent environment. As the reaction progresses, the overall amplitudes of the solute-only term and the cage term decrease due to nongeminate recombination while the amplitudes of the solvent-only term increase due to large volume change caused by the heat release.

In Figure S4A, the difference RDFs of the solute-only term extracted from the TRXL data at various time delays show a single negative peak around 2.85 Å, which indicates the depletion of I–I distance in the parent I_2 molecule. The amplitude of the negative peak nearly disappears in ~10 ns due to the recovery of parent I_2 molecules by nongeminate recombination. Any other kinetic component in the decay dynamics of the negative peak or any shift of the peak position is not observed, indicating the lack of contributions from A/A' state and vibrationally hot X state in this time range. In Figure S4B, the difference RDFs of the cage term extracted from the TRXL data at various time delays have a positive peak at ~4 Å and a negative peak at ~5.5 Å. These features mainly arise from the change of interatomic distances of I–O_{solvent} and I–C_{solvent} atomic pairs. As an I_2 molecule dissociates into two I atoms and a new cage is formed around each I atom, the negative peak is formed at ~5.5 Å, which indicates the depletion of the cage around an I_2 molecule, and the positive peak is formed at ~4 Å, which indicates the formation of a smaller cage around an I atom. The amplitudes of the two peaks also decrease over time due to the recovery of parent I_2 molecules until the peaks disappear completely at 1 μs. The difference RDFs of the solvent-only term is shown in Figure S4C. Since the thermal expansion of the solvent starts only at ~10 ns, the difference RDFs at early time delays before 10 ns are dominated by the temperature change at a constant volume. At the time delay of 1 μs, the average distance between solvent molecules significantly increases due to the volume expansion. As a result, in the difference RDF of the solvent-only term at 1 μs, positive and negative peaks of large amplitudes appear at the positions corresponding to interatomic distances of various atomic pairs in the solvent molecules.

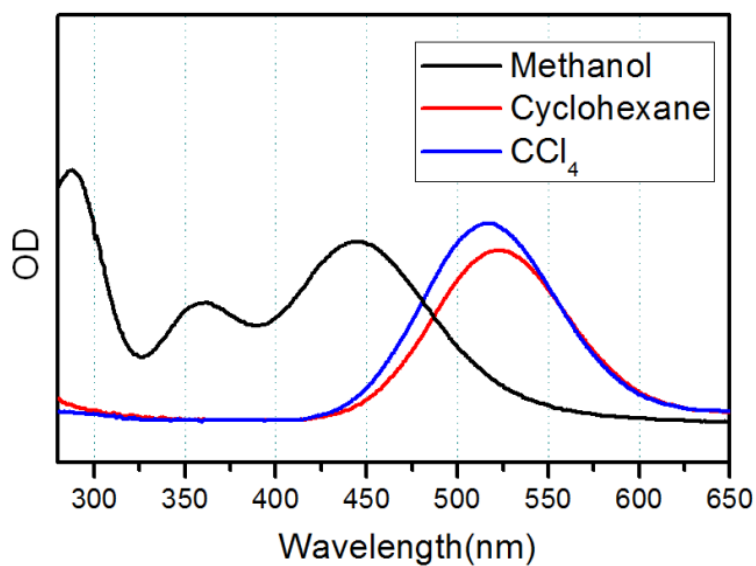


Figure S1. Absorption spectra of I₂ solutions in methanol (black), cyclohexane (red), and CCl₄ (blue). The absorption spectrum of I₂ in methanol is very different from the ones of I₂ in cyclohexane and CCl₄, demonstrating strong influence of solute–solvent interaction on electronic properties and molecular structure of the solute molecules.

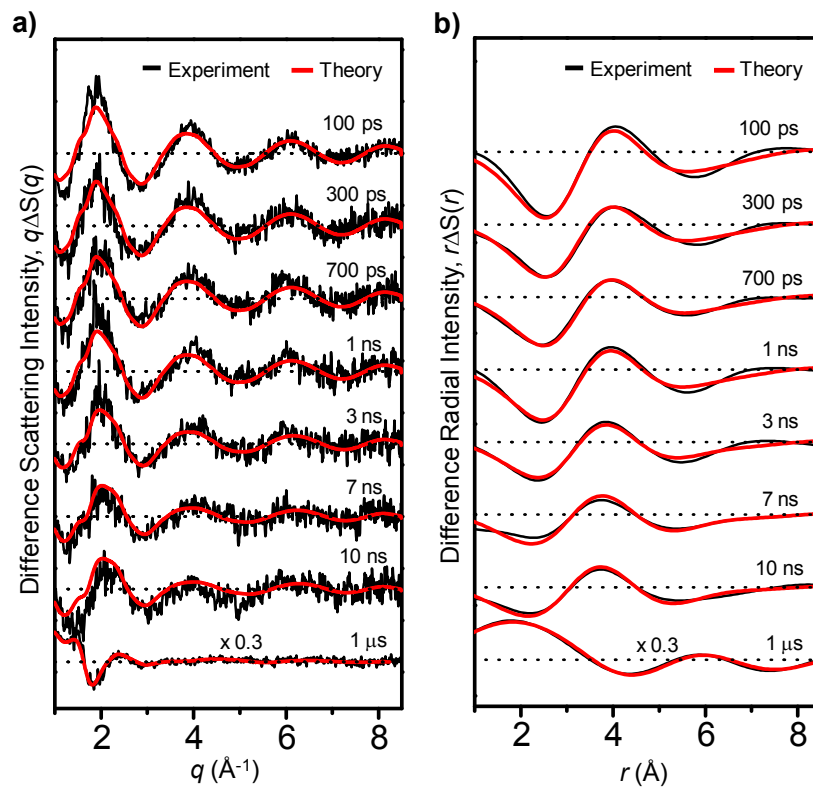


Figure S2. (a) Time-resolved difference X-ray scattering curves, $q\Delta S(q,t)$, measured for the photodissociation of I_2 in methanol. Experimental curves at various time delays (black) and their theoretical fits (red) are shown together. (b) Difference radial distribution functions, $r\Delta S(r,t)$, obtained by sine-Fourier transformation of $q\Delta S(q,t)$ in (a)

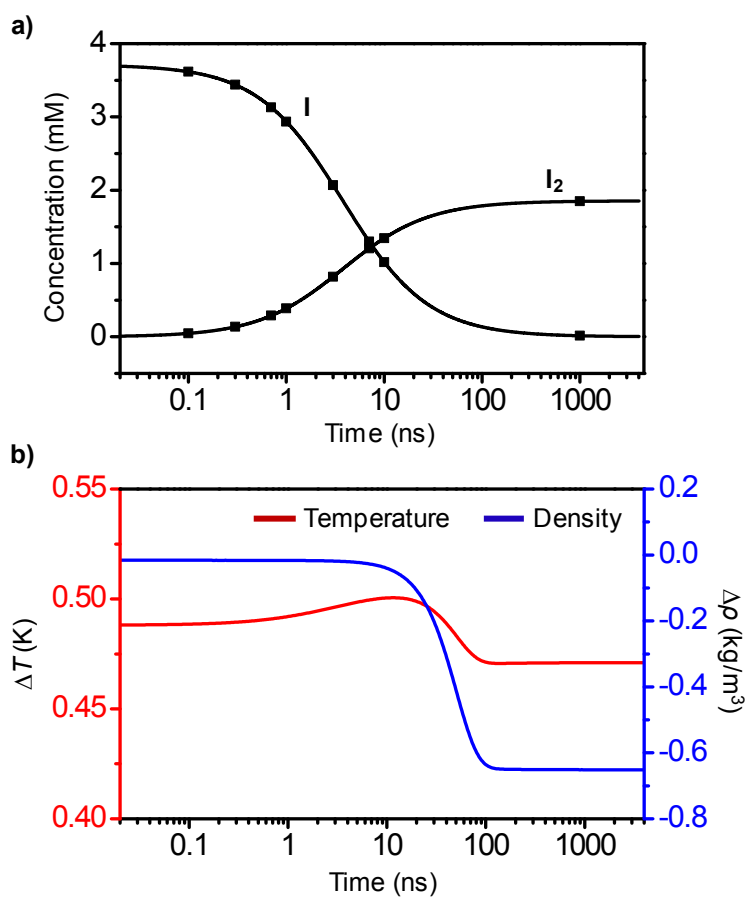


Figure S3. (a) Time-dependent concentration changes of transient solute species after photodissociation of I_2 in methanol. The name of each species is indicated above each time trace. The square points indicate the time delays where the experimental difference scattering curves were measured. (b) Time-dependent changes of solvent temperature (red) and density (blue) after photodissociation of I_2 in methanol.

Figure S4. Reaction mechanism of photodissociation of I₂ in methanol.

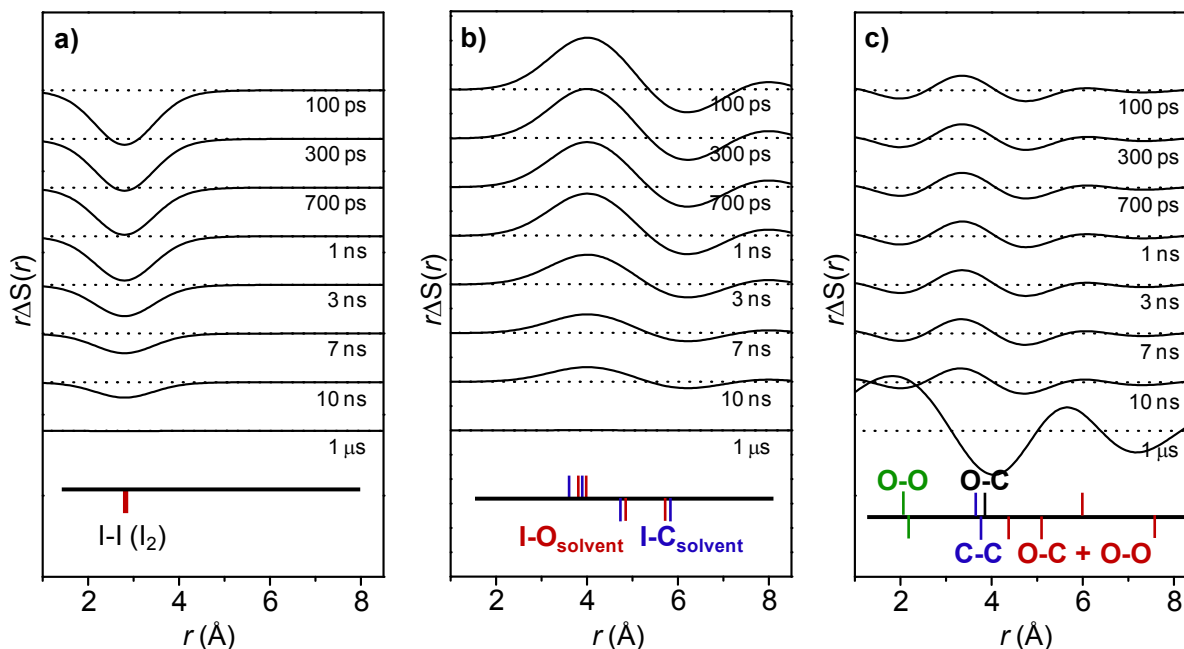


Figure S5. Time-resolved difference radial distribution functions, $r\Delta S(r,t)$, decomposed into three components, (a) the solute-only term, (b) the cage term, and (c) the solvent-only term, for photodissociation of I_2 in methanol. At the bottom of each plot, the distances of major atom-atom pairs are indicated as lines. The lines above the baseline correspond to the positive contributions reflecting the formation of reaction intermediates and products as well as the change in their associated solvent environment, while the lines below the baseline correspond to the negative contributions reflecting the depletion of the reactant (I_2) and the change in its related solvent environment.

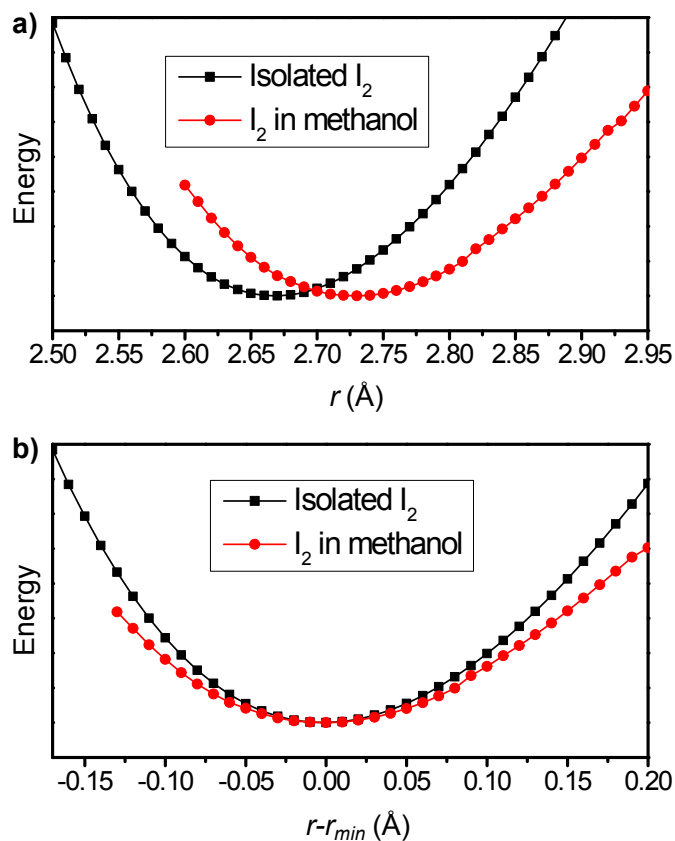


Figure S6. (a) Potential energy curves of isolated I₂ (black) and I₂ in methanol (red) calculated while varying the I–I bond length. For the methanol solution of I₂, the solvent molecules were treated explicitly. The potential energy curve for the isolated I₂ has the minimum energy at $r = 2.67$ Å while the one for I₂ in methanol has the minimum energy at $r = 2.73$ Å. (b) To compare the widths of the two potential energy curves, we converted the r axis to $r - r_{min}$, where $r_{min} = 2.67$ Å and 2.73 Å for the isolated I₂ and the I₂ solution in methanol, respectively. It can be clearly seen that the potential energy curve for I₂ in methanol has a larger width than the one for the isolated I₂, indicating vibrations of larger amplitude and thus weaker I–I bond length of I₂ in methanol.

References

1. H. Ihee, M. Lorenc, T. K. Kim, Q. Y. Kong, M. Cammarata, J. H. Lee, S. Bratos and M. Wulff, *Science*, 2005, **309**, 1223-1227.
2. J. H. Lee, M. Wulff, S. Bratos, J. Petersen, L. Guerin, J. C. Leicknam, M. Cammarata, Q. Kong, J. Kim, K. B. Moller and H. Ihee, *J. Am. Chem. Soc.*, 2013, **135**, 3255-3261.
3. K. Refson, *Comp. Phys. Comm.*, 2000, **126**, 310-329.
4. M. Haughney, M. Ferrario and I. R. McDonald, *J. Phys. Chem.*, 1987, **91**, 4934-4940.
5. M. Cammarata, M. Lorenc, T. K. Kim, J. H. Lee, Q. Y. Kong, E. Pontecorvo, M. Lo Russo, G. Schiro, A. Cupane, M. Wulff and H. Ihee, *J. Chem. Phys.*, 2006, **124**.
6. S. Jun, J. H. Lee, J. Kim, J. Kim, K. H. Kim, Q. Y. Kong, T. K. Kim, M. Lo Russo, M. Wulff and H. Ihee, *Phys. Chem. Chem. Phys.*, 2010, **12**, 11536-11547.
7. J. D. Chai and M. Head-Gordon, *Phys. Chem. Chem. Phys.*, 2008, **10**, 6615-6620.
8. F. Weigend and A. Baldes, *J. Chem. Phys.*, 2010, **133**, 174102.
9. E. Cancès, B. Mennucci and J. Tomasi, *J. Chem. Phys.*, 1997, **107**, 3032-3041.
10. A. L. Harris, J. K. Brown and C. B. Harris, *Annu. Rev. Phys. Chem.*, 1988, **39**, 341-366.
11. N. F. Scherer, D. M. Jonas and G. R. Fleming, *J. Chem. Phys.*, 1993, **99**, 153-168.
12. M. Wulff, S. Bratos, A. Plech, R. Vuilleumier, F. Mirloup, M. Lorenc, Q. Kong and H. Ihee, *J. Chem. Phys.*, 2006, **124**, 034501.